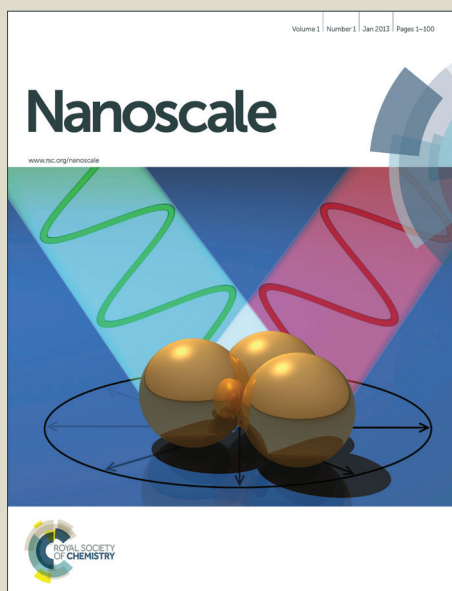


Nanoscale

Accepted Manuscript



This is an *Accepted Manuscript*, which has been through the Royal Society of Chemistry peer review process and has been accepted for publication.

Accepted Manuscripts are published online shortly after acceptance, before technical editing, formatting and proof reading. Using this free service, authors can make their results available to the community, in citable form, before we publish the edited article. We will replace this *Accepted Manuscript* with the edited and formatted *Advance Article* as soon as it is available.

You can find more information about *Accepted Manuscripts* in the [Information for Authors](#).

Please note that technical editing may introduce minor changes to the text and/or graphics, which may alter content. The journal's standard [Terms & Conditions](#) and the [Ethical guidelines](#) still apply. In no event shall the Royal Society of Chemistry be held responsible for any errors or omissions in this *Accepted Manuscript* or any consequences arising from the use of any information it contains.

High mobility flexible graphene field-effect transistors and ambipolar radio-frequency circuits

Yiran Liang, Xuelei Liang*, Zhiyong Zhang, Wei Li, Xiaoye Huo, and Lianmao Peng

Key Laboratory for the Physics and Chemistry of Nanodevices and Department of Electronics,

Peking University, Beijing, 100871, P. R. China

Abstract

Graphene field effect transistors (GFETs) were fabricated on mechanically flexible substrate using chemical vapor deposition graphene. High current density (nearly 200 $\mu\text{A}/\mu\text{m}$) with saturation, almost perfect ambipolar electron-hole behavior, high transconductance (120 $\mu\text{S}/\mu\text{m}$) and good stability in 381 days were obtained. The average carrier mobility for hole (electron) is 13 540 $\text{cm}^2/\text{V}\cdot\text{s}$ (12 300 $\text{cm}^2/\text{V}\cdot\text{s}$) with the highest value over 24 000 $\text{cm}^2/\text{V}\cdot\text{s}$ (20 000 $\text{cm}^2/\text{V}\cdot\text{s}$) was obtained of flexible GFETs. Ambipolar radio-frequency circuits, frequency doubler, were constructed based on the high performed flexible GFET, which show record high output power spectra purity (~97%) and high conversion gain of -13.6 dB. Bending measurements shows the flexible GFETs were able to work under modest strain. These results make flexible GFET a very promising option for future flexible radio-frequency electronics.

Introduction

The demand for flexible electronics grows fast in recent years as it enables special applications with significant commercial potential, such as wearable, bendable and stretchable electronic products, which are difficult to realize with conventional wafer based silicon technology due to its poor mechanical endurance and high-temperature processing. Organic polymer and small molecules are the most conventional building blocks for the flexible electronics due to their intrinsic flexibility or stretchability.¹ However, these materials often have a lower mobility and conductivity.² More importantly, the poor chemical stability in ambient conditions of these conventional materials limits the device lifetime, and thus, their use in practical applications.³

Carbon nanotube (CNT) and graphene are attractive new emerging materials for high performance flexible electronic devices, owing to their superb electrical properties, inert chemical properties and excellent mechanical flexibility. Though the normalized performance of field effect transistors (FETs) built on individual semiconducting CNT has surpassed their silicon counterpart,⁴ the performance of flexible CNT thin film transistor (TFT) is still far behind. High on/off current ratio is easily obtained in CNT-TFTs, which is required for flexible logic circuits. However, the reported mobility of CNT-TFTs are mostly below $100 \text{ cm}^2/\text{V}\cdot\text{s}$.⁵⁻⁹ This is due to they are built on a randomly oriented CNT network with a lot of tube-tube junctions, which limits its electrical properties. The performance of CNT TFTs can be improved by aligning the tubes in the film,¹⁰⁻¹² however, to get large area high density aligned CNT film is still a big challenge. Compared with CNT, graphene is much easier to handle. Large area, up to size of 100 m^2 long,¹³ can be grown by CVD method and transferred onto any target substrate in principle. Though the on/off ratio is low

for graphene FETs, high carrier mobility around 10 000 $\text{cm}^2/\text{V}\cdot\text{s}$ are frequently measured of graphene on common SiO_2/Si substrate at room temperature,¹⁴ and values approaching 100 000 $\text{cm}^2/\text{V}\cdot\text{s}$ has been observed on specially designed rigid substrate (e.g. suspended¹⁵ or using BN as gate dielectrics¹⁶). Such high mobility is desirable for high performance radio-frequency (RF) devices. However, the reported carrier mobility of graphene on flexible substrate is scattered in the range of hundreds to thousands of $\text{cm}^2/\text{V}\cdot\text{s}$,¹⁷⁻³⁴ which is far inferior to its counterparts on rigid substrates. The relatively low carrier mobility on flexible substrates limits the performance of graphene based devices, and hence the application of graphene based flexible electronics.

In this letter, we report high performance flexible graphene field-effect transistors (GFET), showing carrier mobility higher than 10 000 $\text{cm}^2/\text{V}\cdot\text{s}$ on average for both electron and hole, with maximum value over 20 000 $\text{cm}^2/\text{V}\cdot\text{s}$, on flexible polyethylene naphthalate (PEN) substrate. Based on such high performance GFET, high conversion gain (-13.6 dB) frequency doubler with output power spectral purity higher than 97% was realized on flexible substrate. These results obtained on flexible substrates are even better than those on normal SiO_2/Si substrates,^{35, 36} confirming the fast carrier transport is also accessible on polymeric substrate, which is important for pushing the limits of high-speed flexible nanoelectronics.

Experimental results and discussion

Monolayer graphene was synthesized by two-step low pressure chemical vapor deposition (LPCVD) method on a 25 μm thick copper foil substrate.³⁷ The copper foil placed in the quartz-glass tube was first annealed at 1040 $^\circ\text{C}$ in an atmosphere of pure hydrogen with flow of 7

sccm for 20 min., and then 15 sccm mixture gas of CH₄ and Ar (0.5% volume ratio of CH₄) flowed into the quartz-glass tube for 5 min. at the same temperature, designed for the low density nucleation of graphene domains. Then 15 sccm pure CH₄ flowed into chamber at the same temperature for 30 min., replacing the previous mixture gas, for the graphene crystal growing up. After the growth process, it was cooled down quickly. The quality of graphene was characterized by Raman spectroscopy, which was shown in Figure 1. A sharp and symmetric G' peak centered at ~2700 cm⁻¹ with a full width at half maximum (FWHM) ~29 cm⁻¹ is observed, which is roughly 3 times more intense than the G peak at ~1580 cm⁻¹, and no obvious D peak is observed. All these characteristics indicate the graphene is monolayer with high crystalline quality.³⁸

The graphene transfer and devices fabrication processes were shown in Figure 2. The electrochemically delamination method³⁹ was used to transfer the graphene from copper foil onto a flexible substrate. A layer of polymethyl methacrylate (PMMA) was firstly spin coated on the top of graphene for supporting and protection. During the electrochemically delamination, an aqueous solution of NaOH was used as electrolyte solution, and DC voltage about -8 V was applied to the PMMA/graphene/Cu electrode, and the PMMA/graphene film separated from the Cu foil slowly and then floated on the liquid surface of the solution. Subsequently, the PMMA/graphene stack was rinsed with deionized water and then transferred onto 125 μm thick commercial PEN substrate (Dupont Teijin Films Teonex[®] Q65), which was adhered to a rigid glass substrate by *polydimethylsiloxane* (PDMS)³⁴ (*see supporting information*). Then, the PMMA was removed by acetone and the graphene was ready for devices fabrication. Standard photolithography was employed for the GFETs fabrication. Since the flexible PEN substrate was

adhered to rigid substrate, it makes the photolithography process much easier. To avoid the deformation problem of the polymeric substrate, the temperature was controlled below 115 °C during the whole fabrication processes. Firstly, the graphene channel was patterned by oxygen plasma. Then source and drain electrodes were defined by photolithography and the contact area was treated by ultraviolet ozone (UVO), which has been proved to be able to reduce the contact resistance between graphene and the metal electrodes while do not degrade the quality of the underneath graphene.^{40,41} Ti/Au (20 nm/80 nm) was deposited as the source and drain electrodes by electron beam evaporation and followed by lift-off. Yttrium oxide was employed as the gate oxide in this work, because it has been proved to be ideal gate dielectrics for carbon based electronic devices.⁴²⁻⁴⁴ To minimize the substrate deformation, an yttrium film of 2.7 nm thickness was evaporated and oxidized by UVO treatment for 20 min. instead of the usually used thermal oxidation. *The thickness of the oxidized yttrium film is about 4.88 nm measured by atomic force microscope (AFM).* By repeating such process for 3 times, yttrium oxide gate dielectrics with total thickness of 14.6 nm and dielectric constant values ~8 was obtained.⁴² Then, the gate electrode was patterned by photolithography and Ti/Au (20 nm/80 nm) was evaporated and followed by lift-off. Finally, the PEN substrate with devices on it was peeled off the rigid glass substrate. A typical optical image of GFET devices arrays on PEN substrate was also shown in Figure 2.

Figure 3 shows the typical electrical properties of the flexible GFETs by *DC measurement* at room temperature under ambient conditions. Obvious current saturation region was observed before the second linear region in the output curve shown in Figure 3a. Saturation of the drain current leads to large output resistance and hence higher gain with load in RF devices. However, current

saturation of GFET on flexible substrate was reported only by few groups.^{20, 23, 26} As previously reported, thermal constraints of the flexible polymeric substrate restrict the range of applied bias voltage, leading to prevention of strong current saturation.²⁶ But in our work, due to the high gate efficiency using yttrium oxide^{42, 43}, current saturation is easily achieved at relative low bias in the safe operating range, and the flexible GFETs work well with channel current density up to nearly 200 $\mu\text{A}/\mu\text{m}$. Figure 3b shows the transfer curves of the GFET measured at 0.1 V bias. The Dirac point is very close to zero gate voltage, and only minor (~ 20 mV) hysteresis is observed during the gate voltage sweeping back and forth. These indicate a low level charge doping of the graphene during the device fabrication processes and few charge traps existing in the gate dielectric or on the graphene/substrate interface. The peak transconductances for hole and electron conduction are $-32.2 \mu\text{S}/\mu\text{m}$ and $23.5 \mu\text{S}/\mu\text{m}$, respectively. The maximum transconductance increases with the source-drain bias (shown in the inset of Figure 3b), which reaches to $120 \mu\text{S}/\mu\text{m}$ at 0.5 V bias and the transfer curve is still very symmetric for electron and hole conduction at this bias. The output current density and the normalized transconductance are among the best reported results of GFET on flexible substrate,^{17, 19, 29} especially when taking the relative large channel area of our devices ($4 \mu\text{m}$ wide and $6 \sim 10 \mu\text{m}$ long) into account. The carrier mobility was firstly estimated using peak transconductance method with the formula of $\mu = (L_g/C_g \cdot V_{ds}) \cdot g_m$, where L_g is the gate length, C_g is the capacitance per unit length, V_{ds} is the bias and g_m is the peak transconductance. Though it is known that the mobility is greatly underestimated by using the peak transconductance method due to the contact resistance effect, it gives quick evaluation of the performance of the fabricated devices. The obtained mobility values are $4173 \text{ cm}^2/\text{V}\cdot\text{s}$ for hole and $3046 \text{ cm}^2/\text{V}\cdot\text{s}$ for electron of the device in Figure 3 (a, b), respectively. These values are

among the best reported results for the GFET on flexible substrate (as shown in Table 1), which indicate the intrinsic performance of our devices should be much better. To obtain the intrinsic carrier mobility, the measured transfer property was fitted using a widely accepted diffusive transport model.⁴⁵ The access resistance R_a of the nonaligned graphene between the top gate and the contact (as shown in Figure 4a), as well as the S/D contact resistance R_c , were included into the series resistance R_s in this fitting model⁴⁶. The extracted values for hole and electron are 18 056 $\text{cm}^2/\text{V}\cdot\text{s}$ and 13 346 $\text{cm}^2/\text{V}\cdot\text{s}$ respectively, as shown in Figure 3c. *The normalized series resistance is 5.68 $\text{k}\Omega\cdot\mu\text{m}$ and 5.89 $\text{k}\Omega\cdot\mu\text{m}$ for hole and electron respectively, and the residual carrier concentration $n_0 = 1.31 \times 10^{11}/\text{cm}^2$. The low residual carrier concentration reflects that the graphene suffers few contaminants after the multiple fabrication process.* Statistics of the carrier mobility of 32 devices was shown in Figure 3d, and the values of most devices are distributed in the range of 8 000~ 20 000 $\text{cm}^2/\text{V}\cdot\text{s}$. The highest mobility for hole (electron) is over 24 000 $\text{cm}^2/\text{V}\cdot\text{s}$ (20 000 $\text{cm}^2/\text{V}\cdot\text{s}$) with average of 13 540 $\text{cm}^2/\text{V}\cdot\text{s}$ (12 300 $\text{cm}^2/\text{V}\cdot\text{s}$). These values are significantly higher than the previously reported works on flexible substrates which were listed in Table 1, and are even better than the highest mobility for GFETs on SiO_2/Si substrates.^{14, 47, 48} The high-mobility suggests that the good electrical quality of graphene is neither substantially impacted by the device fabrication process, nor significantly impacted by the gate oxide or substrate scattering. *The scattered distribution of the mobility values in Fig. 3d was attributed to the growth inhomogeneity of the CVD grown graphene. It is known that the CVD grown graphene are polycrystalline,³⁷ and grain boundaries and defects distribute randomly. This will cause crystalline quality fluctuation of the graphene channel in the GFETs and hence the fluctuation of the measured carrier mobility.*

The electric transport properties of graphene are affected by many factors, such as the growth and transfer quality of the graphene, the substrate roughness, and interfacial charge traps or phonons. Raman measurement in Figure 1 proved the high growth quality of the graphene used in our work. We have studied the transfer technique of CVD graphene extensively and clean and almost crackless transfer of CVD graphene can be routinely achieved in our group.^{39, 49} To obtain a clean graphene surface, PMMA used for transfer and photo resist used in the device fabrication process were carefully removed in each fabrication step. Besides, we believe that the flexible substrate used in this work contributes importantly to the obtained high carrier mobility. The Teonex®Q65 substrate possesses excellent thermal stability that a level of shrinkage down to 25 ppm can be achieved at 150 °C.⁵⁰ Since the temperature is controlled below 115 °C in our device fabrication process, the substrate deformation and thermal stress in the graphene are negligible. The inherent surface roughness of the substrate is less than 1 nm,⁵⁰ which is comparable to the normal SiO₂ substrate. Figure 4 shows the typical AFM image of our GFET on PEN substrate as well as the surface roughness of each part of the device. The graphene channel area, including the S/D/G metal electrodes covered parts, is very smooth. However, outside the channel area, the surface roughness of the substrate and the S/D/G metal on substrate directly, are pretty high, ~20 nm. This is understandable because oxygen plasma causes damage to the polymeric substrate surface during graphene channel patterning that will lead to a rough electrodes surface. Meanwhile, the roughness of the whole graphene channel area, as measured from both the metal electrodes covered part and the un-gated channel part, is less than 3 nm. It should be mentioned that the un-gated channel area was covered with yttrium oxide in fact. Considering the original surface roughness of PEN is less

than 1 nm, the yttrium oxide thickness is around 15 nm and the growth method of the yttrium oxide, one can deduce that clean and smooth interfaces of the PEN/graphene/Yttrium oxide sandwich structure was achieved. Such clean and smooth interfaces, as well as the low level charge traps in the gate dielectric and interfaces mentioned above, are all favor for reducing scattering and hence leading to the high carrier mobility. Otherwise, it is known that graphene devices fabricated on SiO₂ substrate suffer from additional scattering associated with low-energy surface phonon *and trapped charge in SiO₂*.^{51, 52} A polymeric substrate, e.g. PEN, *has been considered be able to mitigate the degradation caused by the trapped charge* and cause lower surface phonon scattering to the carrier in graphene as compared with rigid substrate (e.g. SiO₂).²¹ We believe these also contribute to the high mobility observed in this work. However, more detailed work is needed to elucidate this effect.

GFETs were also fabricated on the PET substrate as a comparison, using the same graphene transfer and device fabrication processes. However, the obtained mobility values by diffusive transport model of most devices are in the range of several hundred to two thousand cm²/V·s with the highest value of 3110 cm²/V·s for hole and 2708 cm²/V·s for electron (Figure S1 in the supporting information). *The relatively lower mobility of graphene on PET substrate was ascribed to two reasons. Firstly, the surface of PET substrate we used is rougher than PEN. Secondly, as mentioned before, the PEN substrate has much better thermal stability than PET which results in lower substrate deformation and thermal stress in graphene. It can be seen from Table 1 that the relatively high performance GFETs are more likely achieved on the PEN substrate.* These results indicate the choice of flexible substrate also impact the performance of GFETs.

The top-gate GFETs on PEN substrate show pretty good reliability during a period of 381 days, which is important for practical application. As shown in Figure 5, the device works well 381 days after device fabrication, though the Dirac point in the transfer curve shifts slightly towards positive value. This is understandable that water or oxygen molecules in air may permeate through the yttrium oxide or the PEN substrate during such a long time, and hence lead to a more pronounced p-type behavior. Though the obtained carrier mobility decreases about 20-30 % relatively, the absolute values are still higher than $7500 \text{ cm}^2/\text{V}\cdot\text{s}$ for both hole and electron, which are still better than most of the results in Table 1.

All the excellent electrical properties discussed above, current saturation with high density, high transconductance, symmetric electron-hole behavior and extremely high carrier mobility, suggest that our GFETs on PEN are very promising for flexible RF application. Here we demonstrate this concept by constructing a frequency doubler (shown in Figure 6), which is an important device for communication system. For a 10 KHz input sinusoidal signal with an amplitude of 300 mV, the output signal with amplitude $\sim 62.5 \text{ mV}$ was shown in Figure 6b. The conversion gain is -13.6 dB and the output power -14.08 dBm. When the frequency of the input signal increased to 11 MHz, the GFET based frequency doubler still functioned well as shown in Figure 6c. The conversion gain is -17.7 dB, with an output power of -18.17 dBm. The output power spectrum, obtained by analyzing the Fourier transform of the output signal, is shown in Figure 6d. For the 10 KHz input signal, more than 96.6% of the output power is concentrated at the doubled fundamental frequency of 20 kHz, and more than 97.7% of the output power is concentrated at the desired 22 MHz for the 11 MHz input signal. The spectra purity and conversion gain are the most important parameters of

a frequency doubler. These two values of our devices are the best reported results for graphene-based flexible frequency doubler to our knowledge.²³ *However, the performance of the GFET based frequency doubler in this work is still far from optimization. We believe the conversion gain and the output power can be much improved and the working frequency can be up to gigahertz once the GFET structure and fabrication process were optimized.*

Bending measurement of the electrical properties of the flexible GFETs was carried out by attaching the flexible substrate onto lateral surface of cylindrical supporting brackets with different radius, and the dependence of device performance on the bending radius is shown in Figure 7. The infinity symbol ∞ in the abscissa indicates flat conditions (no bending of the substrate). It needs to be noticed that the substrate bending was parallel to the source/channel/drain direction (the transport direction), as it is the critical direction most impacted by the mechanical strain.⁵³ The graphene transistors maintained functionality with the bending radius down to ~ 7.8 mm. This radius corresponds to a mechanical strain of 8‰, which is sufficient for most application environment of flexible devices. An average increase of the total source/drain resistance, $\sim 25\%$, at zero gate voltage was detected as seen in Figure 7b. The resistance increase is owing to the mechanical deformation and the elongation of both the metal electrode and channel material, as well as the reconstruction of interfaces in the device.²⁴ Figure 7c shows that the Dirac voltage shifted ~ 0.2 V towards the negative voltage as compared with the flat condition. *This is consistent with the reported effect of strain on the work function of graphene.*⁵⁴ Shown in Figure 7d is the mobility change with the bending radius. The hole mobility (μ_p) increases slightly with bending at first and then tends to saturate. However, the electron mobility (μ_n) shows an opposite trend, which decreases with bending at first and then tends to saturate. *Similar*¹⁸ *and even opposite*¹⁹

results were also reported, however the underlying mechanism is still an open issue. This is due to that strain may affect the band structure and work function of graphene⁵⁴ and hence the p-n junction in the graphene channel near the electrodes.⁵⁵ Gate capacitance also changes⁵⁶ with strain, which affects the coupling of gate to electron and hole. Therefore, more detailed work is needed to elucidate all these effects, which is beyond the scope of this paper. Further bending of the substrate below the radius of 7.8 mm led to failure of the devices. Once the bending was released and the devices were measured again at flat conditions, they recovered. Such failure is caused by the broken of the relatively thick metal or the relatively brittle gate dielectrics instead of the graphene channel area⁵⁷, which has also been reported previously.^{22,24} Approach for mitigating this type of device failure has been proposed,⁵⁸ and currently we are working on this.

Summary

In summary, GFETs were fabricated on flexible substrate using chemical vapor deposition graphene. By combining appropriate substrate (PEN in this work) and device fabrication process (low temperature yttrium oxide growth), high current density with saturation, high transconductance and extremely high carrier mobility was obtained, which also show pretty good stability. A frequency doubler was constructed using the flexible GFET, which shows record high spectra purity and high conversion gain. The flexible GFETs were confirmed to be able to working under modest strain by bending test. Considering the device in this work is still far from optimization, we believe that the performance of the flexible GFET can be further enhanced, which indicates a bright future of graphene based flexible RF electronics.

Acknowledgement

This work was supported by the Ministry of Science and Technology of China (Grant No. 2011CB921904), the Ministry of education of China (Grant No. 113003A), Natural Science Foundation (NSF) of China (Grant No. 61321001, 61390504 and 61427901), and Beijing Municipal Science and Technology Commission (Grant No. Z141100003814006).

Table 1 Comparison of carrier mobility of reported flexible GFET. Unit: $\text{cm}^2/\text{V}\cdot\text{s}$.

Reference	Graphene type	Substrate	Gate dielectric	Mobility (hole/electron)	Mobility extraction method
17	CVD	PI	Al_2O_3 (ALD)	4930/1130	Diffusive transport model
18	CVD	PET	Graphene oxide	150/116	Peak transconductance method
19	CVD	PET	Ion gel	$203 \pm 57/91 \pm 50$	Peak transconductance method
20	CVD	PET	Al_2O_3 (natural)	~ 3000 , max < 5000	Diffusive transport model
21	CVD	PET	Al_2O_3 (natural)	2000~8000 300/230	Diffusive transport model Peak transconductance method
22	CVD	PI	Al_2O_3 (ALD)	2800/3900	Diffusive transport model
23	CVD	PI	h-BN	2324/2307	Diffusive transport model
24	CVD	PI	Al_2O_3 (ALD)	1400	Diffusive transport model
25	CVD	PET	Ion gel	$892 \pm 196/628 \pm 146$	Diffusive transport model
26	CVD	PEN	HfO_2 (ALD)	~ 1500	Peak transconductance method
27	CVD	PDMS	Ion gel	$1188 \pm 136/422 \pm 52$	Diffusive transport model
28	CVD	PEN	Al_2O_3 (ALD)	$3342 \pm 26/2813 \pm 11$	Diffusive transport model
29	Solution	PI	YO_x	102 ± 19	Peak transconductance method
30*	Exfoliated	PET	PMMA	10000/4000	Peak transconductance method
31	CVD	PET	PMMA	630/370	Peak transconductance method
32	CVD	PEN	$\text{Al}_2\text{O}_3/\text{HfO}_x/\text{Al}_2\text{O}_3$	67($\pm 10\%$)	Peak transconductance method
33	CVD	PI	Al_2O_3 (ALD)	1100/2200	Diffusive transport model
34#	CVD	PEN	Al_2O_3 (ALD)	9214/12980	Diffusive transport model(pulse I-V)
This work	CVD	PEN	YO_x	13540/12300(average)	Diffusive transport model
				24000/21000(max)	Diffusive transport model
				4173/3046	Peak transconductance method

Note: * Though high mobility is obtained by peak transconductance method measured in Ref. 30, it is exfoliated graphene.

The mobilities extracted from DC I-V curve are 4154/7016 $\text{cm}^2/\text{V}\cdot\text{s}$ for hole/electron in Ref. 34, which are much lower than those extracted from the pulse I-V measurement.

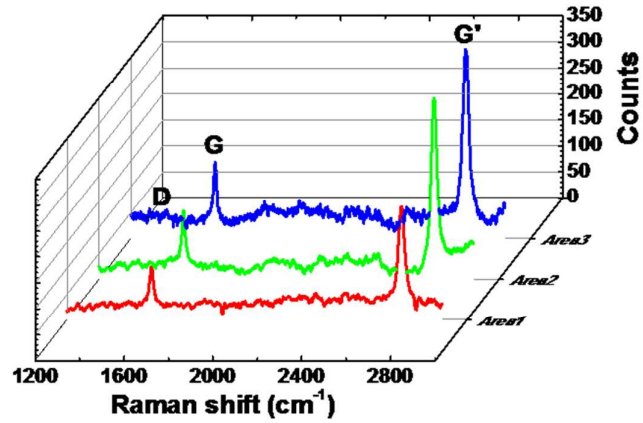


Figure 1 Typical Raman spectrum of the graphene grown on Cu foil, using a laser source with the wavelength of 488 nm.

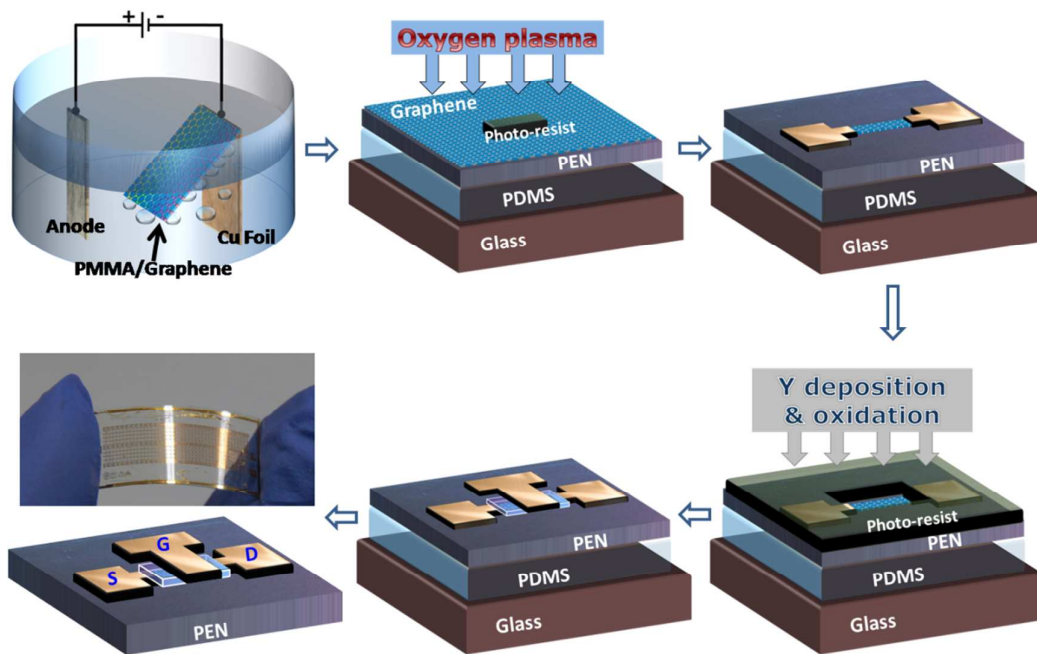


Figure 2 Schematic of the graphene transfer and GFET fabrication processes.

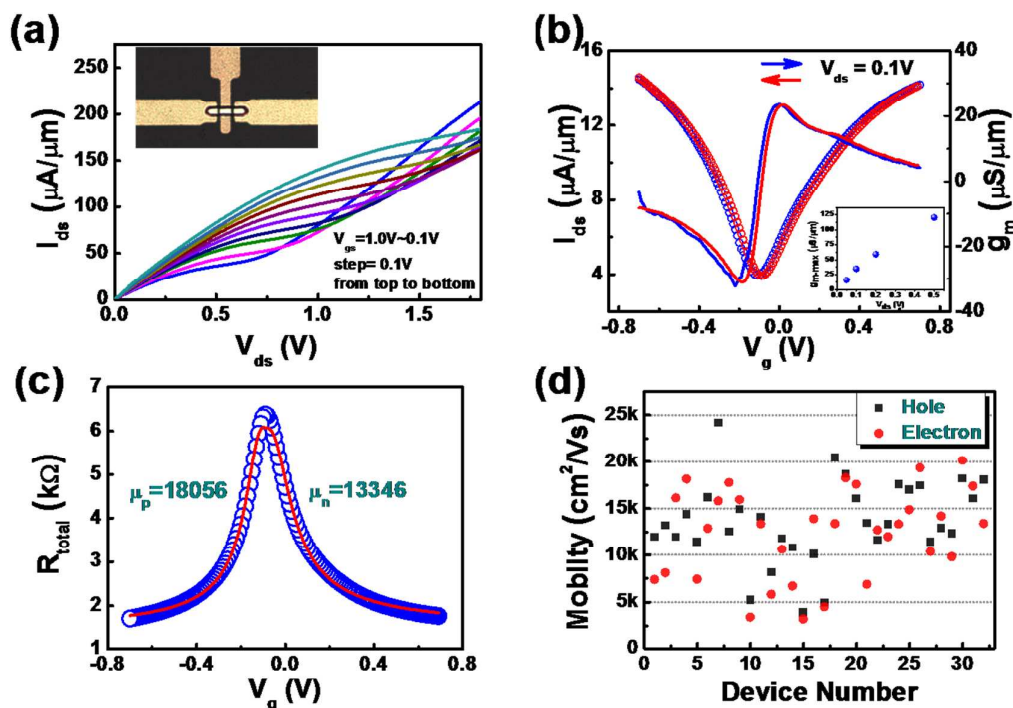


Figure 3(a) Typical out-put properties of flexible GFET with channel area of $4 \mu\text{m}$ wide and $6.26 \mu\text{m}$ long. (b) Corresponding transfer property and transconductance of the GFET in (a), $V_{ds}=0.1 \text{ V}$. Inset: bias dependence of the transconductance. (c) Carrier mobility extraction using diffusive model, $V_{ds}=0.1 \text{ V}$. (d) Statistics of the carrier mobility.

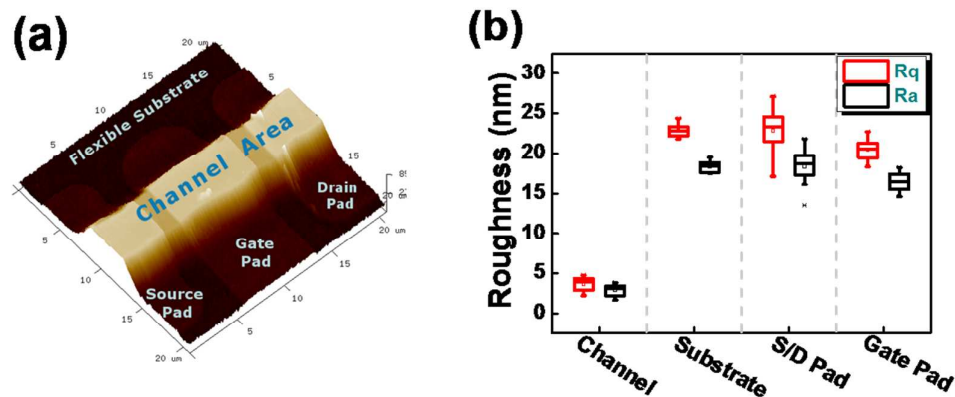


Figure 4 (a) AFM image of typical GFET on PEN substrate. (b) The average roughness (Ra) and the root mean square roughness (Rq) of each part of the GFET. Roughness of channel were measured from both the metal electrodes covered part and the un-gated channel part, and those for the S/D/G electrodes were measured in the area of metal directly on substrate.

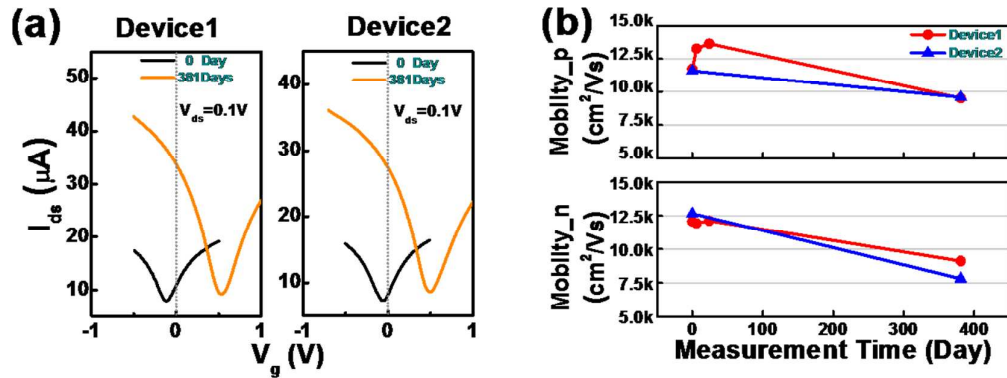


Figure 5 Reliability of the flexible GFET. (a) Comparison of transfers curve of two typical devices pre and post 381 days after the device fabrication. (b) Carrier mobility (by diffusive transport model) change vs. measurement time.

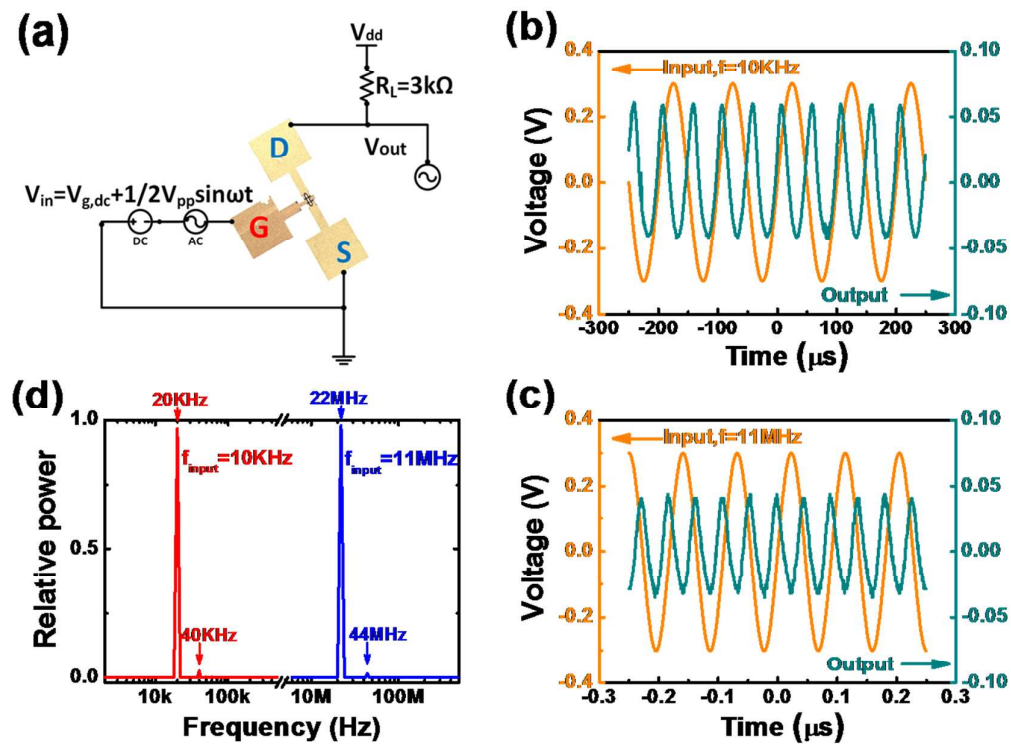


Figure 6 Measurement of the graphene frequency doubler. (a) Circuit diagram of the GFET based frequency doubler. Output signal measurements of the frequency doubler at input of 10 KHz (b)

and 11 MHz (c). (d) Corresponding output power spectrum.

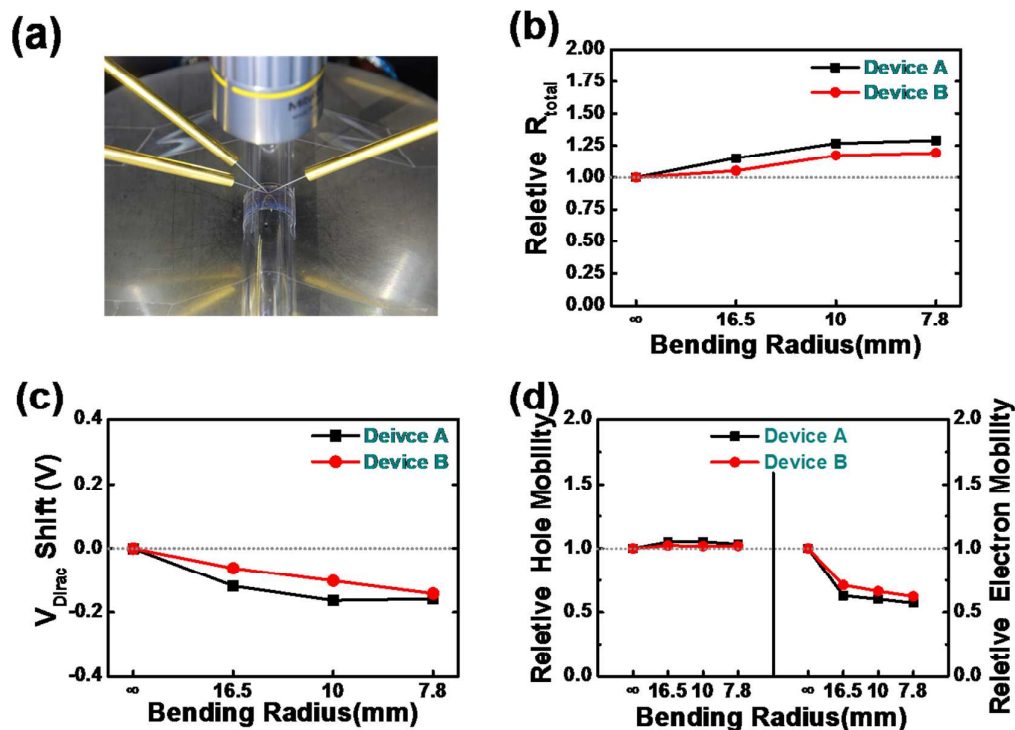


Figure 7 Bending test of the flexible GFETs. (a) Photograph of the measurement setup. Typical dependence of the R_{total} (b), V_{Dirac} (c) and mobility of hole and electron (d), on the bending radius.

References

1. F. Garnier, A. Yassar, R. Hajlaoui, G. Horowitz, F. Deloffre, B. Servet, S. Ries and P. Alnot, *Journal of the American Chemical Society*, 1993, **115**, 8716-8721.
2. S. Logothetidis and A. Laskarakis, *Thin Solid Films*, 2009, **518**, 1245-1249.
3. B. A. Jones, M. J. Ahrens, M.-H. Yoon, A. Facchetti, T. J. Marks and M. R. Wasielewski, *Angewandte Chemie*, 2004, **116**, 6523-6526.
4. A. D. Franklin, M. Luisier, S.-J. Han, G. Tulevski, C. M. Breslin, L. Gignac, M. S. Lundstrom and W. Haensch, *Nano Lett.*, 2012, **12**, 758-762.
5. C. Wang, J. Zhang and C. Zhou, *ACS Nano*, 2010, **4**, 7123-7132.
6. C. Wang, J.-C. Chien, K. Takei, T. Takahashi, J. Nah, A. M. Niknejad and A. Javey, *Nano Lett.*, 2012, **12**, 1527-1533.
7. V. K. Sangwan, R. P. Ortiz, J. M. P. Alaboson, J. D. Emery, M. J. Bedzyk, L. J. Lauhon, T. J. Marks and M. C. Hersam, *ACS Nano*, 2012, **6**, 7480-7488.
8. C. Wang, A. Badmaev, A. Jooyaie, M. Bao, K. L. Wang, K. Galatsis and C. Zhou, *ACS Nano*, 2011, **5**, 4169-4176.
9. D.-m. Sun, M. Y. Timmermans, Y. Tian, A. G. Nasibulin, E. I. Kauppinen, S. Kishimoto, T. Mizutani and Y. Ohno, *Nat Nano*, 2011, **6**, 156-161.
10. Q. Cao, S.-j. Han and G. S. Tulevski, *Nature communications*, 2014, **5**.
11. G. J. Brady, Y. Joo, M.-Y. Wu, M. J. Shea, P. Gopalan and M. S. Arnold, *ACS Nano*, 2014, **8**,

- 11614-11621.
12. Q. Cao, S.-J. Han, G. S. Tulevski, Y. Zhu, D. D. Lu and W. Haensch, *Nature nanotechnology*, 2013, **8**, 180-186.
 13. T. Kobayashi, M. Bando, N. Kimura, K. Shimizu, K. Kadono, N. Umezu, K. Miyahara, S. Hayazaki, S. Nagai, Y. Mizuguchi, Y. Murakami and D. Hobara, *Applied Physics Letters*, 2013, **102**, 023112.
 14. S. Rahimi, L. Tao, S. F. Chowdhury, S. Park, A. Jouvray, S. Buttress, N. Rupesinghe, K. Teo and D. Akinwande, *Acs Nano*, 2014, **8**, 10471-10479.
 15. K. I. Bolotin, K. J. Sikes, J. Hone, H. L. Stormer and P. Kim, *Physical Review Letters*, 2008, **101**, 096802.
 16. C. R. Dean, A. F. Young, Mericl, LeeC, WangL, SorgenfreiS, WatanabeK, TaniguchiT, KimP, K. L. Shepard and HoneJ, *Nat Nano*, 2010, **5**, 722-726.
 17. J. Lee, L. Tao, Y. Hao, R. S. Ruoff and D. Akinwande, *Applied Physics Letters*, 2012, **100**, 152104.
 18. S.-K. Lee, H. Y. Jang, S. Jang, E. Choi, B. H. Hong, J. Lee, S. Park and J.-H. Ahn, *Nano Lett.*, 2012, **12**, 3472-3476.
 19. B. J. Kim, H. Jang, S. K. Lee, B. H. Hong, J. H. Ahn and J. H. Cho, *Nano Lett.*, 2010, **10**, 3464-3466.
 20. C.-H. Yeh, Y.-W. Lain, Y.-C. Chiu, C.-H. Liao, D. R. Moyano, S. S. H. Hsu and P.-W. Chiu, *ACS nano*, 2014, **8**, 7663-7670.
 21. C.-C. Lu, Y.-C. Lin, C.-H. Yeh, J.-C. Huang and P.-W. Chiu, *Acs Nano*, 2012, **6**, 4469-4474.
 22. J. Lee, T.-J. Ha, H. Li, K. N. Parrish, M. Holt, A. Dodabalapur, R. S. Ruoff and D. Akinwande, *ACS Nano*, 2013, **7**, 7744-7750.
 23. L. JongHo, H. Tae-Jun, K. N. Parrish, S. F. Chowdhury, T. Li, A. Dodabalapur and D. Akinwande, *Electron Device Letters, IEEE*, 2013, **34**, 172-174.
 24. J. Lee, L. Tao, K. N. Parrish, Y. F. Hao, R. S. Ruoff and D. Akinwande, *Applied Physics Letters*, 2012, **101**.
 25. B. J. Kim, S. K. Lee, M. S. Kang, J. H. Ahn and J. H. Cho, *Acs Nano*, 2012, **6**, 8646-8651.
 26. N. Petrone, I. Meric, J. Hone and K. L. Shepard, *Nano Lett.*, 2012, **13**, 121-125.
 27. S.-K. Lee, B. J. Kim, H. Jang, S. C. Yoon, C. Lee, B. H. Hong, J. A. Rogers, J. H. Cho and J.-H. Ahn, *Nano Lett.*, 2011, **11**, 4642-4646.
 28. S. Lee, K. Lee, C.-H. Liu, G. S. Kulkarni and Z. Zhong, *Nature communications*, 2012, **3**, 1018.
 29. C. Sire, F. Ardiaca, S. Lepilliet, J. W. T. Seo, M. C. Hersam, G. Darnbrine, H. Happy and V. Derycke, *Nano Lett.*, 2012, **12**, 1184-1188.
 30. J. H. Chen, M. Ishigami, C. Jang, D. R. Hines, M. S. Fuhrer and E. D. Williams, *Advanced Materials*, 2007, **19**, 3623-3627.
 31. J. Meng, J.-J. Chen, L. Zhang, Y.-Q. Bie, Z.-M. Liao and D.-P. Yu, *Small*, 2014, DOI: 10.1002/sml.201402422, n/a-n/a.
 32. S. M. Kim, E. B. Song, S. Lee, J. Zhu, D. H. Seo, M. Mecklenburg, S. Seo and K. L. Wang, *ACS Nano*, 2012, **6**, 7879-7884.
 33. M. E. Ramon, K. N. Parrish, L. Jongho, C. W. Magnuson, T. Li, R. S. Ruoff, S. K. Banerjee and D. Akinwande, presented in part at the 2012 IEEE/MTT-S International Microwave Symposium - MTT 2012, 2012.
 34. S. Lee, O. D. Iyore, S. Park, Y. G. Lee, S. Jandhyala, C. G. Kang, G. Mordi, Y. Kim, M. Quevedo-Lopez, B. E. Gnade, R. M. Wallace, B. H. Lee and J. Kim, *Carbon*, 2014, **68**, 791-797.
 35. H. Wang, D. Nezich, J. Kong and T. Palacios, *Electron Device Letters, IEEE*, 2009, **30**, 547-549.
 36. Z. Wang, Z. Zhang, H. Xu, L. Ding, S. Wang and L.-M. Peng, *Applied Physics Letters*, 2010, **96**, 173104.
 37. X. Li, C. W. Magnuson, A. Venugopal, J. An, J. W. Suk, B. Han, M. Borysiak, W. Cai, A. Velamakanni, Y. Zhu, L. Fu, E. M. Vogel, E. Voelkl, L. Colombo and R. S. Ruoff, *Nano Lett*, 2010, **10**, 4328-4334.
 38. A. C. Ferrari, J. C. Meyer, V. Scardaci, C. Casiraghi, M. Lazzeri, F. Mauri, S. Piscanec, D. Jiang, K. S. Novoselov, S. Roth and A. K. Geim, *Physical Review Letters*, 2006, **97**, 187401.
 39. L. B. Gao, W. C. Ren, H. L. Xu, L. Jin, Z. X. Wang, T. Ma, L. P. Ma, Z. Y. Zhang, Q. Fu, L. M. Peng, X. H. Bao and H. M. Cheng, *Nature communications*, 2012, **3**, 699.
 40. W. Li, Y. Liang, D. Yu, L. Peng, K. P. Pernstich, T. Shen, A. R. Hight Walker, G. Cheng, C. A. Hacker, C. A. Richter, Q. Li, D. J. Gundlach and X. Liang, *Applied Physics Letters*, 2013, **102**,

- 183110-183110-183115.
41. W. Li, C. A. Hacker, G. Cheng, Y. Liang, B. Tian, A. R. Hight Walker, C. A. Richter, D. J. Gundlach, X. Liang and L. Peng, *Journal of Applied Physics*, 2014, **115**, 114304.
 42. Z. Wang, H. Xu, Z. Zhang, S. Wang, L. Ding, Q. Zeng, L. Yang, T. Pei, X. Liang, M. Gao and L.-M. Peng, *Nano Letters*, 2010, **10**, 2024-2030.
 43. H. Xu, Z. Zhang, H. Xu, Z. Wang, S. Wang and L.-M. Peng, *ACS Nano*, 2011, **5**, 5031-5037.
 44. L. Wang, X. L. Chen, Y. Wang, Z. F. Wu, W. Li, Y. Han, M. W. Zhang, Y. H. He, C. Zhu, K. K. Fung and N. Wang, *Nanoscale*, 2013, **5**, 1116-1120.
 45. S. Kim, J. Nah, I. Jo, D. Shahrjerdi, L. Colombo, Z. Yao, E. Tutuc and S. K. Banerjee, *Applied Physics Letters*, 2009, **94**, 062107.
 46. D. B. Farmer, Y.-M. Lin and P. Avouris, *Applied Physics Letters*, 2010, **97**, 013103.
 47. L. Liao, J. W. Bai, Y. Q. Qu, Y. C. Lin, Y. J. Li, Y. Huang and X. F. Duan, *Proceedings Of the National Academy Of Sciences Of the United States Of America*, 2010, **107**, 6711-6715.
 48. H. Jinseong, C. Hyun-Jong, L. Sung-Hoon, Y. Heejun, S. Jaikwang, U. I. Chung and S. Sunae, *2011 69th Annual Device Research Conference (DRC)*, 2011, DOI: 10.1109/drc.2011.5994407, 31-32.
 49. X. Liang, B. A. Sperling, I. Calizo, G. Cheng, C. A. Hacker, Q. Zhang, Y. Obeng, K. Yan, H. Peng, Q. Li, X. Zhu, H. Yuan, A. R. H. Walker, Z. Liu, L.-m. Peng and C. A. Richter, *Acs Nano*, 2011, **5**, 9144-9153.
 50. W. A. MacDonald, M. K. Looney, D. MacKerron, R. Eveson, R. Adam, K. Hashimoto and K. Rakos, *J. Soc. Inf. Disp.*, 2007, **15**, 1075-1083.
 51. S. Fratini and F. Guinea, *Physical Review B*, 2008, **77**, 195415.
 52. J.-H. Chen, C. Jang, S. Xiao, M. Ishigami and M. S. Fuhrer, *Nat Nano*, 2008, **3**, 206-209.
 53. K. S. Kim, Y. Zhao, H. Jang, S. Y. Lee, J. M. Kim, K. S. Kim, J. H. Ahn, P. Kim, J. Y. Choi and B. H. Hong, *Nature*, 2009, **457**, 706-710.
 54. S.-M. Choi, S.-H. Jhi and Y.-W. Son, *Physical Review B*, 2010, **81**, 081407.
 55. F. N. Xia, V. Perebeinos, Y. M. Lin, Y. Q. Wu and P. Avouris, *Nature Nanotechnology*, 2011, **6**, 179-184.
 56. G. S. Kliros, *Nanoscale Research Letters*, 2014, **9**, 65.
 57. M. Huang, T. A. Pascal, H. Kim, W. A. Goddard and J. R. Greer, *Nano Lett.*, 2011, **11**, 1241-1246.
 58. D. H. Kim, J. H. Ahn, W. M. Choi, H. S. Kim, T. H. Kim, J. Z. Song, Y. G. Y. Huang, Z. J. Liu, C. Lu and J. A. Rogers, *Science*, 2008, **320**, 507-511.

Supporting Information

Formation of the PEN/PDMS/rigid substrate structure:

The PDMS base and curing agent were mixed thoroughly with the mass ratio of 10:1, and the mixture was put into a bell-jar dessicator and pumped to remove the air bubble. The clear and bubble free PDMS mixture was spin coated on the rigid substrate with speed of 4000 rpm. Then the PEN film was adhered onto the PDMS surface, and the PEN/PDMS/rigid substrate stack was baked on the hotplate at 115 °C for 10 minutes to cure the PDMS film.

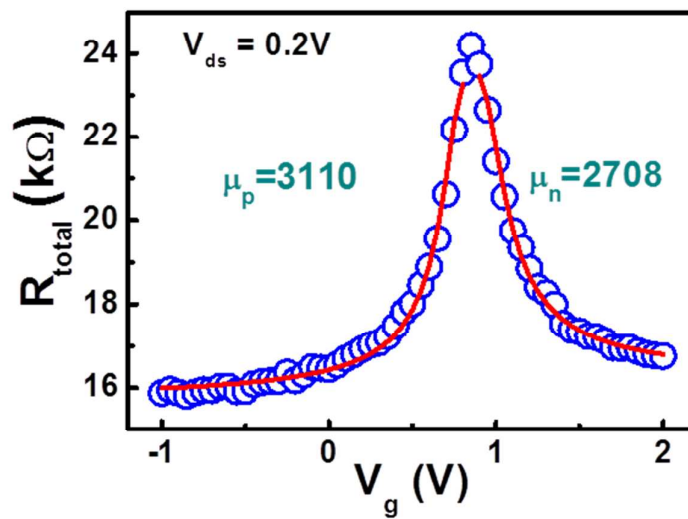


Figure S1 Mobility extraction using the diffusive transport model for device fabricated on PET substrate.